AIAA SciTech Forum
6-10 January 2025, Orlando, FL
AIAA SCITECH 2025 Forum

10.2514/6.2025-2494

A 3-D Laser-Fluid Interaction Solver Within the OpenFOAM Framework

Vikramank Singh *, Kowsik Bodi † and Aniruddha Sinha.‡
Indian Institute of Technology Bombay, Mumbai, Maharashtra, 400076

The utility and power of lasers have been continuously increasing. High-energy lasers interact with the fluid medium through which they pass, leading to laser beam distortion. This thermal distortion of the laser beam within the beam delivery system affects the quality of the laser and poses challenges in designing high-power laser beam delivery systems. To numerically study the laser-fluid interaction within such systems, we developed a 3-D laser-fluid solver in the OpenFOAM toolbox. While most existing computational studies address the beam distortion during propagation in open atmosphere, this paper focuses on what happens within a confined domain. The details and validation of the solver are presented. The solver effectively captures the physical phenomena observed in the literature and demonstrates accuracy in simulating beam behavior and fluid response. The results are consistent with theoretical predictions and experimental findings.

I. Introduction

High energy lasers find various industrial applications such as cutting, welding, and heat treatment [1, 2]. They also hold potential for diverse fields, including laser propulsion and wireless power transmission [3, 4]. When a high-energy laser beam propagates through a fluid medium, the fluid medium gets heated due to the absorption of the laser beam photons by the molecules of the medium. This heating changes the fluid's temperature and thus its density and refractive index. The changed refractive index of the fluid medium then distorts the laser beam passing through it which again affects the fluid's refractive index. Thus, the laser beam intensity distribution in the three dimensional space and the refractive index of the medium affect each other in a coupled manner. The presence of natural convection due to gravity complicates this laser-fluid interaction which results in laser beam deterioration.

Initially, when the convection effects are insignificant, the refractive index decreases due to the expansion of the fluid in the laser's path, forming a negative lens. This results in the swelling of the beam profile, a phenomenon known as thermal blooming. Thermal blooming is a well-reported phenomenon [5]. In the open atmosphere, significant laser-fluid interaction studies have been carried out [5–8]. These studies considered beam distortion in presence of transverse wind. The presence of external flow or wind modifies the fluid dynamics of the medium because the thermal convection effect of the applied flow dominates other effects. This simplifies the computation by imposing wind or another external flow. Using similar techniques, some studies have been done by changing the fluid medium to seawater and rain [9, 10]. Recently Akers et al. solved the 2-D fluid dynamics along with laser to study the laser beam distortions [11].

Within the laser beam delivery system, after the beam production, the laser beam passes through various optical systems that adjust its size and direction before it exits out of the beam director's window [12, 13]. While travelling between the mirrors and lenses inside the beam director, the laser beam interacts with the fluid and gets distorted. The mitigation of laser distortions inside the beam delivery systems will aid in developing efficient and more powerful high energy laser devices.

To investigate laser-fluid interactions within a closed domain and account for three-dimensional fluid dynamics, we have developed a solver, icoLfiFoam, in the OpenFOAM environment. The novelty of the work lies in the implementation of the laser propagation solver coupled with a conventional finite volume flow solver, as well as its application to laser-fluid interaction in confined spaces.

*PhD student, Department of Aerospace Engineering, vikramankpratapsingh@gmail.com.
†Associate Professor, Department of Aerospace Engineering, AIAA Member.
‡Associate Professor, Department of Aerospace Engineering, AIAA Member.

II. Mathematical Formulation

Our objective is to simulate the interaction between the laser beam and the fluid medium as it propagates between two optical systems within a beam director. We model a section of the beam director, between these two optical systems, as a closed domain. In this domain, the laser enters at one end, passes through the fluid medium, and exits at the opposite end. The laser beam properties at the exit are the primary metrics of interest. In the computational domain, the fluid adheres to physical boundary conditions, while the laser remains sufficiently distant from the side walls along the beam propagation direction.

Given practical conditions and laser power, the temperature increase caused by the absorption of a continuous laser beam propagating through the fluid is minimal. Fluid dynamics is thus governed by the incompressible Navier-Stokes equations under the Boussinesq approximation [14]:

$$\nabla \cdot \mathbf{u} = 0, \tag{1a}$$

$$\frac{\partial \mathbf{u}}{\partial t} + (\mathbf{u} \cdot \nabla)\mathbf{u} = \nu \nabla^2 \mathbf{u} - \frac{1}{\rho_0}\nabla p + \frac{T - T_0}{T_0}\mathbf{g}, \tag{1b}$$

$$\frac{\partial T}{\partial t} + (\mathbf{u} \cdot \nabla)T = \alpha \nabla^2 T + s. \tag{1c}$$

In the energy equation, a source term s is added to account for the temperature increase resulting from laser absorption by the fluid medium. Here, $\mathbf{u}$ represents velocity, p represents pressure, T represents temperature, ν is the kinematic viscosity, α is the thermal diffusivity, while T_0 and ρ_0 respectively represent initial temperature and density of the medium. Additionally, $\mathbf{g}$ refers to gravitational acceleration.

The propagation of the laser beam through the fluid medium under the paraxial approximation ($|\partial A/\partial z| \ll |kA|$) is described by the paraxial equation (see Appendix A):

$$2ik\frac{\partial A}{\partial z} = A_{xx} + A_{yy} + k^2\left(\frac{n^2}{n_0^2} - 1\right)A - ik\beta A. \tag{2}$$

Here, z is the direction of beam propagation, while x and y are the orthogonal directions. The local (complex) amplitude of the laser is denoted by A, and i is the square root of negative unity. Beam intensity and amplitude are related by $I = |A|^2$. The wave number of the beam is denoted by k, while $n(x, y, z; t)$ represents the refractive index of the medium, and n_0 represents the initial ($t = 0$) refractive index of the medium. The refractive index and temperature are related using the following relation (see Appendix B):

$$\frac{n^2}{n_0^2} - 1 = 2\frac{(T - T_0)}{n_0}\frac{dn}{dT}. \tag{3}$$

Here, dn/dT is a property of the medium, representing the rate of change of refractive index with temperature. It is typically a negative value, meaning the refractive index decreases as the temperature increases.

Volumetric heat absorption rate by the fluid medium due to the laser heating is βI, where β is the absorption coefficient of the medium. Hence, the corresponding rate of temperature change in the medium due to laser heating is given by:

$$s = \frac{\beta}{\rho_0 c_p} I, \tag{4}$$

where c_p denotes the specific heat capacity of the fluid.

III. Solution Methodology

The solution of equations 1 and 2 with the appropriate initial and boundary conditions yields results for laser-fluid interaction. We selected icoFoam, a validated transient incompressible laminar flow solver within the OpenFOAM library for solving the fluid dynamics [15]. It solves the Navier-Stokes equations using the PISO algorithm [16]. OpenFOAM is structured to handle any time dependent partial differential equation (PDE) having convection, diffusion and source terms [17]. The paraxial equation is a complex PDE, parabolic in the z-direction, and it does not have any

time dependence (i.e., since the laser propagation time scale is minuscule relative to the flow time scale). We split the paraxial equation of variable $A = A_r + iA_i$ into two PDEs of real variables A_r and A_i.

$$2k\frac{\partial A_r}{\partial z} = A_{ixx} + A_{iyy} + k^2\left(\frac{n^2}{n_0^2} - 1\right)A_i - k\beta A_r, \tag{5a}$$

$$2k\frac{\partial A_i}{\partial z} = -A_{rxx} - A_{ryy} - k^2\left(\frac{n^2}{n_0^2} - 1\right)A_r - k\beta A_i. \tag{5b}$$

Equations 2, and hence, Eq. 5a, 5b are parabolic equations that are solved numerically by marching along the beam propagation direction, i.e., z. To the best of the authors' knowledge, OpenFOAM does not have in-built modules that allow this space-marching approach. Hence, we explicitly added the computation of the paraxial equation within the icoLfiFoam solver using basic C++ syntax.

Since the source term $k^2(n^2/n_0^2 - 1)A$ is k times larger than the $2ik(\partial A/\partial z)$ term, where k is a very large value, the paraxial equation exhibits stiffness. We used the split-step spectral method to solve the paraxial equation [18, 19]. First, the source terms are integrated analytically over Δz. Then, the x- and y- derivatives are calculated in the spectral domain and are integrated over Δz using the values obtained by the integration of source terms. In a compact form, the method can be expressed as:

$$A(x, y, z + \Delta z; t) = \mathcal{F}^{-1}\left(\mathcal{F}\left(A(x, y, z; t)\exp\left(k^2\left(\frac{n^2}{n_0^2} - 1\right)\frac{\Delta z}{2ik} - \frac{\beta_a \Delta z}{2}\right)\right)\exp\left(-\frac{(k_x^2 + k_y^2)\Delta z}{2ik}\right)\right). \tag{6}$$

k_x and k_y represent the wavenumbers in the x and y directions, respectively. The operators $\mathcal{F}$ and $\mathcal{F}^{-1}$ denote the forward and inverse Fourier transforms in the x and y directions. These operations are executed within the icoLfiFoam solver using the FFTW library [20]. Thus, the paraxial equation is solved in two separate steps. Each step is highly accurate, but a small error is introduced due to their separate computation. We verified the numerical implementation of the split-step method by testing it on the 1-D nonlinear Schrodinger Equation (NLSE) (see Appendix C).

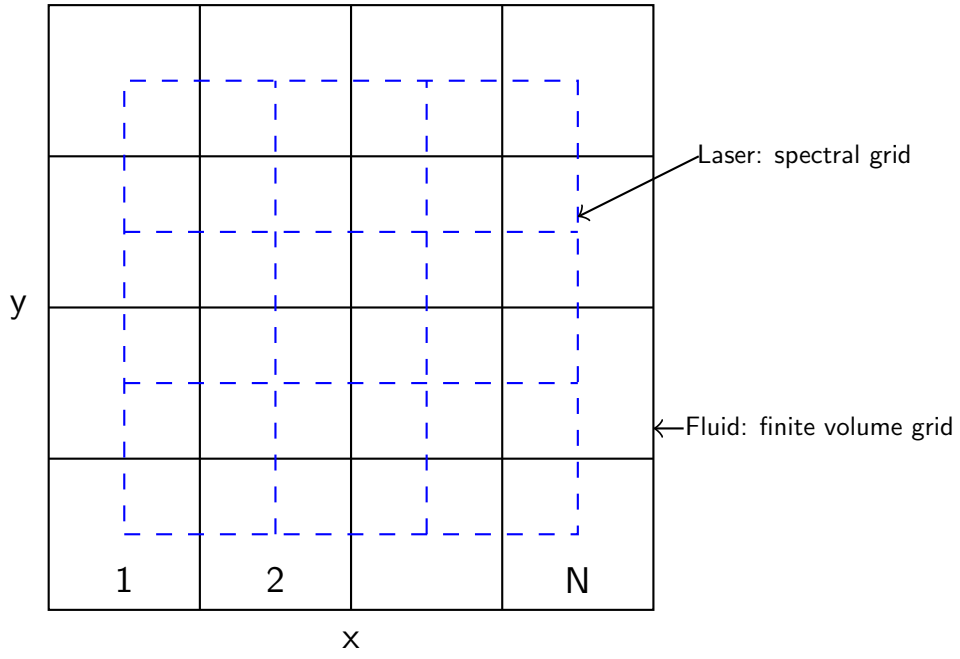

Fig. 1 Laser-fluid grid in the plane perpendicular to the beam propagation direction.

While the spectral method is a node based method, OpenFOAM solves fluid variables at the cell centers using the finite volume method. To ensure compatibility, the grid nodes for the paraxial equation variable coincide with the cell

centers of the grid for the fluid variables in the x, y directions as represented in Fig. 1. The laser grid is periodic, with the laser amplitude solved at each z plane on $(N-1)\times(N-1)$ nodes. The laser domain is truncated by half a grid size at both ends in the x and y directions. Since the laser remains far from the side walls, the laser amplitude drops to zero near the walls, eliminating the need for additional boundary treatments. The laser amplitude at the N^{th} nodes is assumed to be equal to its value on the respective 1^{st} nodes in the x and y direction. The fluid at the $(j+1)^{\text{th}}$ time step is solved using the laser intensity field at the j^{th} time step, and the laser amplitude is corrected at the $(j+1)^{\text{th}}$ time step using the temperature field at the same step.

The incoming laser beam profile serves as the initial condition at the first stencil plane (xy) along the z-direction, as shown in Fig. 2. To compute the laser amplitude at the $z+\Delta z$ location, the refractive index used is calculated using the average temperature between the z and $z+\Delta z$ planes.

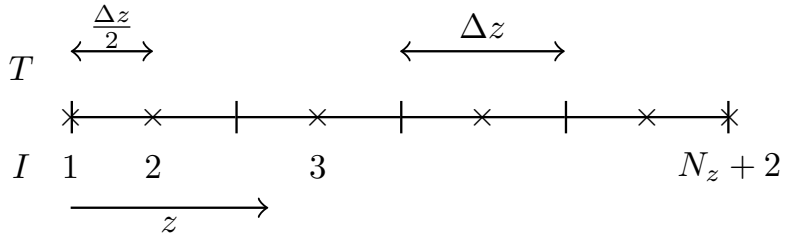

Fig. 2 Computational stencil along the beam propagation direction.

IV. Results

A. Vacuum propagation

When a laser beam propagates through a vacuum, diffraction causes the beam to diverge. At the source ($z=0$), the intensity of a Gaussian beam is defined as

$$I(x,y,0;t) = I_0 \mathrm{e}^{-\frac{x^2+y^2}{r^2}}. \tag{7}$$

Here, I_0 represents the peak laser intensity at the source and r represents the laser beam's initial radius (between 1 and 1/e intensity points). It is calculated using the laser power at source, P_0 and the radius using the relation (see Appendix D)

$$I_0 = \frac{P_0}{\pi r^2}. \tag{8}$$

For a continuous Gaussian beam of wavelength λ, radius r, propagating through a medium of constant refractive index n, laser beam intensity distribution after propagating through distance z is [21]

$$I(x,y,z) = I_0 \left(\frac{r}{r(z)}\right)^2 \exp\left(-\frac{x^2+y^2}{r(z)^2}\right). \tag{9}$$

Here,

$$r(z) = r\sqrt{1+\left(\frac{z\lambda}{2\pi r^2 n}\right)^2} \tag{10}$$

is the beam radius at distance z.

For a laser beam of power 11 W, wavelength of 10.6 µm and radius of 1.4 mm, the intensity profile after propagating for 0.5 m through a vacuum ($n=1$) was calculated using the laser-fluid solver. We used a computational domain of size 1.2 cm × 1.2 cm × 50 cm discretized into a $201\times201\times40$ grid. The laser beam was sourced at $x=0$, $y=0$ in the $z=0$ plane. At the end of the domain ($z=50$ cm), the numerical results were compared to the analytical solution, showing good agreement, as illustrated in Fig. 3. Since the medium is vacuum, the values of all fluid dynamic variables are zero.

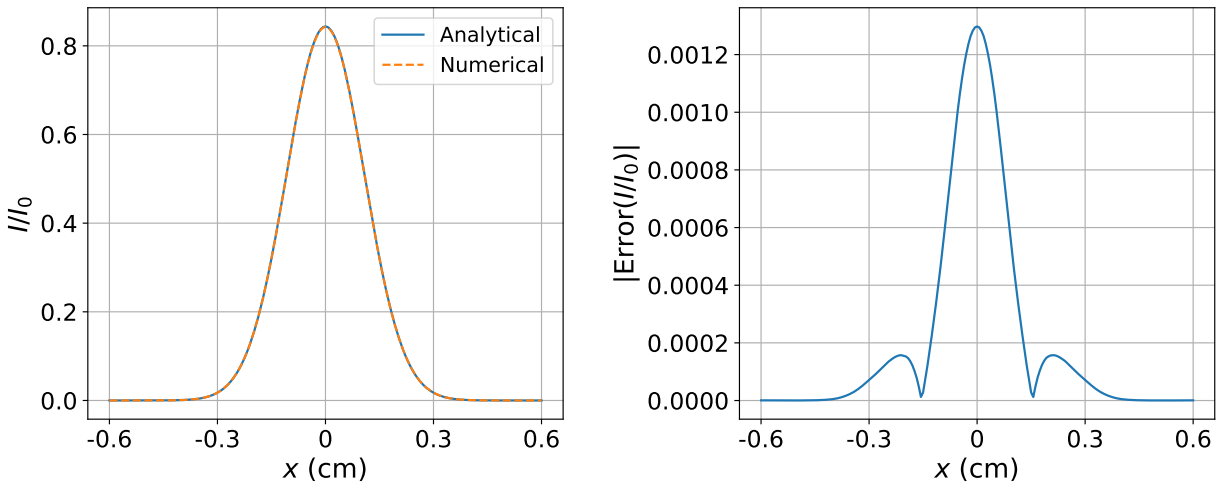

Fig. 3 Comparison of numerical and analytical solutions for laser beam propagation in a vacuum. Plots of I/I_0 and the absolute error in I/I_0 at $y = 0, z = 50$ cm as functions of x.

B. Laser fluid interaction

Another validation of the developed laser-fluid solver is conducted based on the laser thermal distortion experiment by Gebhardt et al. [22]. In their experiment, a laser beam is directed through a high-absorptivity fluid in a cylindrical cell of 5 cm diameter and 2.5 cm length. The cell is made to move at a constant speed perpendicular to the laser beam propagation direction. The resulting laser distortion has been reported. To replicate their experiment, for ease of computation we have taken a cuboid-shape computational domain of dimensions $L_x \times L_y \times L_z$ as shown in Fig. 4, where L_x, L_y, and L_z are the domain lengths along x, y and z axes respectively. The dimensions of the cuboid are taken as $L_x = L_y = 3.54$ cm. (which is $1/\sqrt{2}$ times the diameter of the cylindrical cell used in the reference experiment) and $L_z = 2.5$ cm, inscribing the cuboid within the cylindrical cell's dimensions.

In this setup, a continuous Gaussian laser beam with a wavelength of 10.6 µm and a radius of 1.4 mm is introduced from the $z = 0$ plane. The fluid medium is CS_2, having thermophysical and optical properties as mentioned in Table 1. This fluid has an exceptionally high absorption coefficient, which leads to significant beam distortion over a short propagation path, even with a laser beam of modest power. The laser beam is moving with respect to the domain along the negative x direction. All the boundaries of the fluid domain are considered as free-slip, isothermal wall. We have considered free-slip walls since we are not interested in resolving the boundaries especially along the z direction. Based on our numerical trials, free-slip, isothermal walls provided better stability. Moreover, the experimental domain is a cylindrical cell whereas our computational domain is a cuboid, which implicitly discounts any significant wall boundary effects.

Table 1 Thermophysical and optical properties of the fluid medium.

$dn/dT(\mathrm{K}^{-1})$	α ($\mathrm{m}^2\mathrm{s}^{-1}$)	ν ($\mathrm{m}^2\mathrm{s}^{-1}$)	$\beta(\mathrm{m}^{-1})$	$c_p(\mathrm{Jkg}^{-1}\mathrm{K}^{-1})$	n_0	$\rho_0(\mathrm{kgm}^{-}3)$	$T_0(\mathrm{K})$
-0.79×10^{-3}	1.25×10^{-7}	2.86×10^{-7}	25.2	950	1.63	1260	300

The laser beam has an initial power of 11 W and a velocity relative to the fluid domain of 0.9 cm/s. After conducting a grid independence test, as shown in Fig. 5, we have selected a $601 \times 601 \times 40$ uniform grid. The beam distortion parameter, N_D, defined by Gerhardt et al. is calculated using the formula [22]:

$$N_D = \frac{-2dn/dT I_0 L_z}{n_0 \rho_0 c_p u r} \left(1 - \frac{1 - \mathrm{e}^{-\beta_a L_z}}{\beta_a L_z}\right). \tag{11}$$

Here, u is the velocity of laser relative to the fluid domain and is perpendicular to the beam propagation direction. It should be noted that for the simulation parameters considered in this work, the calculated value of N_D is approximately 0.74, whereas for the experiment it is reported as 0.7.

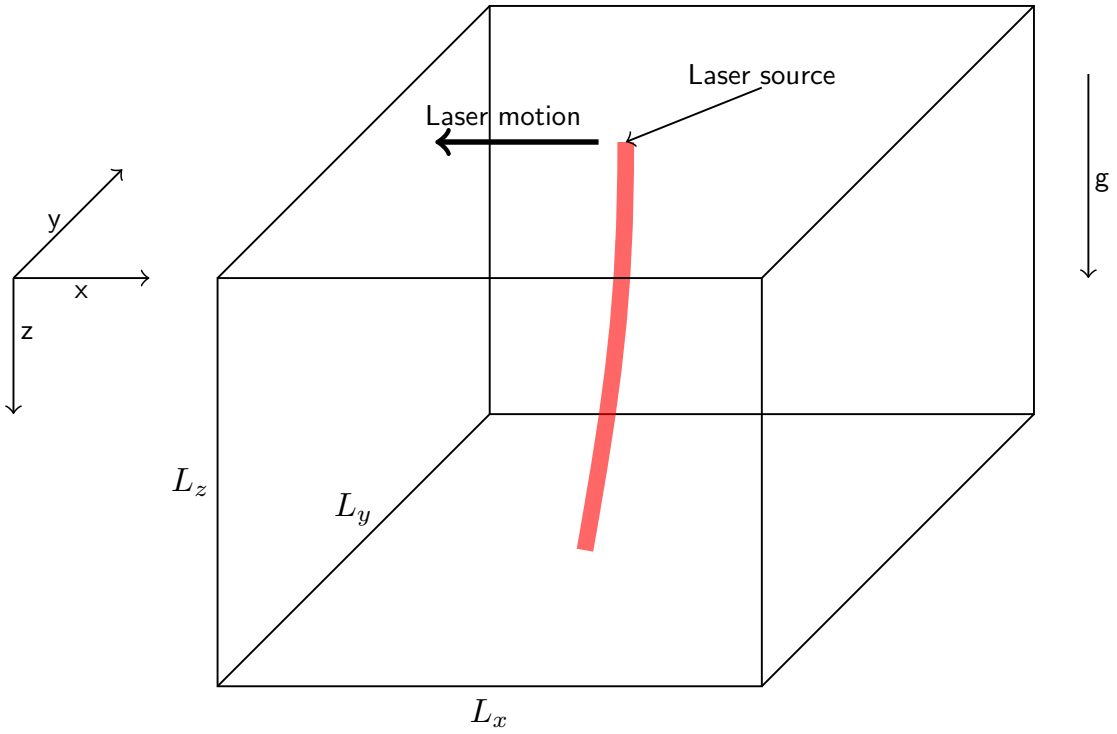

Fig. 4 Illustration of the computational domain for moving laser problem.

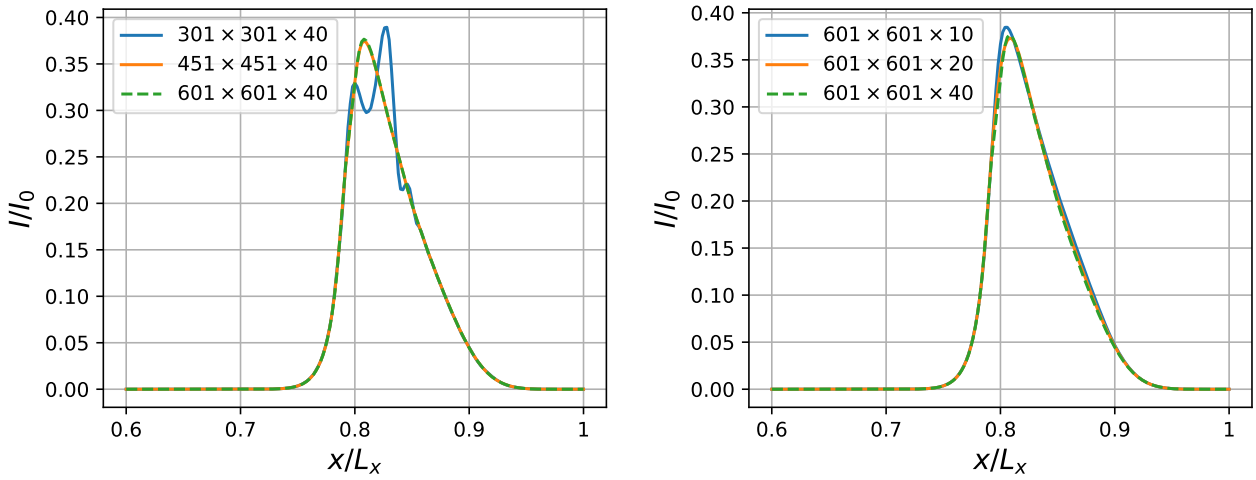

Fig. 5 Grid independence test in the xy and z directions in terms of the x-profile of the laser at the bottom wall ($y = Ly/2$, $z = L_z$) at t = 0.3 s. By this time, significant laser beam distortion has occurred, as shown in Fig. 6.

At the start of the simulation (t = 0 s), the laser beam source is positioned at the mid xz plane ($y = L_y/2$) near the right wall, as shown in Fig. 4. The laser beam starts moving in the xz plane from right to left until it reaches the left wall. As the laser beam passes through the fluid medium, the fluid is heated due to the absorption of photons. This heating increases the temperature along the beam's path, causing the beam to experience thermal blooming. The swelling of the laser beam's cross-section relative to its initial state can be observed in Fig. 6. The laser beam continues to move forward (right to left) over time, leaving behind a heated region. The temperature profile at a time t = 1.5 s is shown in Fig. 7. In the forward direction, the beam encounters cooler fluid, as it has just arrived in that region, while on the backward side, the fluid temperature is higher since the beam has previously passed through that region. Since

refractive index decreases with increase in temperature ($dn/dT < 0$), and light bends towards the region with higher refractive index, we observe the beam skewing in the forward direction. Laser beam intensity profile evolution with time along the beam path is shown in Fig. 8. Due to gravity, the hot fluids are convected upwards. The convection currents carry the heat with them, and colder fluid enters the beam path from below. These convection currents thus reduce the strength of the temperature gradient that was built up by the combined effects of laser heating and beam motion. Therefore, in this experiment, convection reduces the beam distortion.

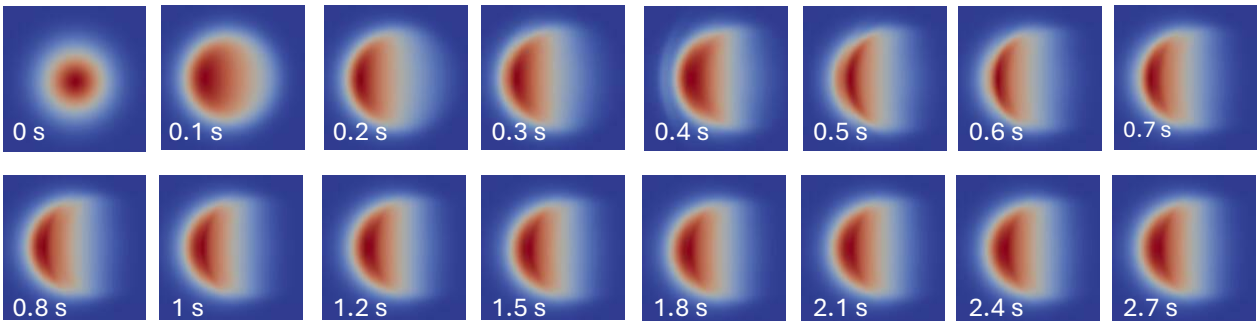

Fig. 6 Laser intensity profile evolution with time in the $z = L_z$ plane. For better visibility of the beam profile, each image has its own scale.

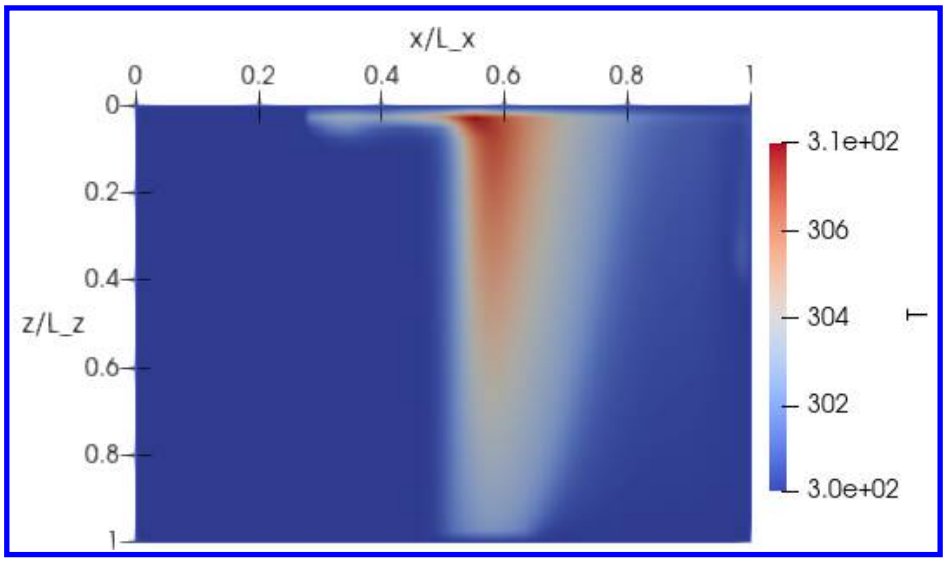

Fig. 7 Temperature profile in the $y = Ly/2$ plane at t = 1.5 s. The laser moves from right to left.

The peak intensity value of the laser beam in the exit plane is represented by I_p. The evolution of laser beam peak intensity with time in the $z = L_z$ plane is plotted in Fig. 9(a). The peak intensity due to thermal blooming initially decreases rapidly, and then increases due to the beam skewing towards the direction of beam motion. At $t = 0.6$ s, we observe a local maximum in the peak intensity value, which then begins to decrease again. The peak intensity value appears to attain steady-state after $t = 1.2$ s. After $t = 2.5$ s, as the beam approaches the left wall, we observe a dip in the peak intensity due to wall effects.

The laser beam travels parallel to the z-direction. In the absence of distortion, the beam center (in terms of x and y coordinates) at both the inlet and exit planes would coincide. The distance between the location of peak intensity at the exit plane and the beam center at the inlet plane represents the beam deflection, denoted by Δx. The normalized beam deflection $\Delta x/r$ as a function of time is shown in Fig. 9(b). Initially undeflected, the beam deflects rapidly in the direction of its motion. At $t = 0.2$ s, the normalized beam deflection value reaches 0.8. Following fluctuations until $t = 1.3$ s, the deflection value nearly stabilizes around 0.6. The laser moves on a discrete grid, with a grid size

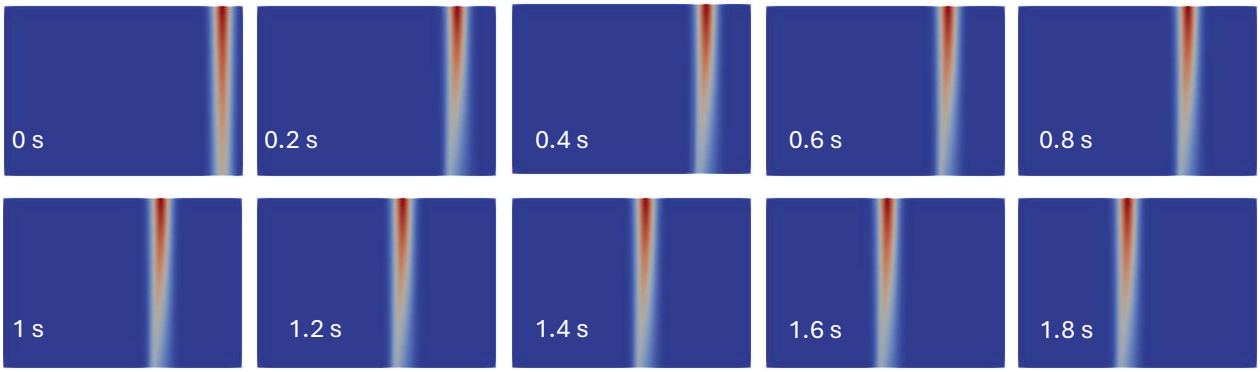

Fig. 8 Laser beam intensity along its path over time in the $y = L_y/2$ plane, with the full xz domain displayed. The laser is directed from top to bottom.

in the xy plane relative to the beam radius of 0.042, which is significant compared to the beam deflection. Quadratic interpolation was employed to determine the beam deflection values. At the start of the experiment, heating causes convection currents to move upwards, and the hot fluid hits the upper wall of the domain, where it is then deflected around the laser path. As a result, some hot fluid regions precede the laser path, reducing laser beam skewing, and we observe a dip in both peak intensity and deflection after a short time. The average beam deflection behavior aligns with physical expectations. The details of these transients probably depend on the formulation of the boundary conditions at the inlet and outlet walls; however, the long-term behavior may be expected to be robustly simulated.

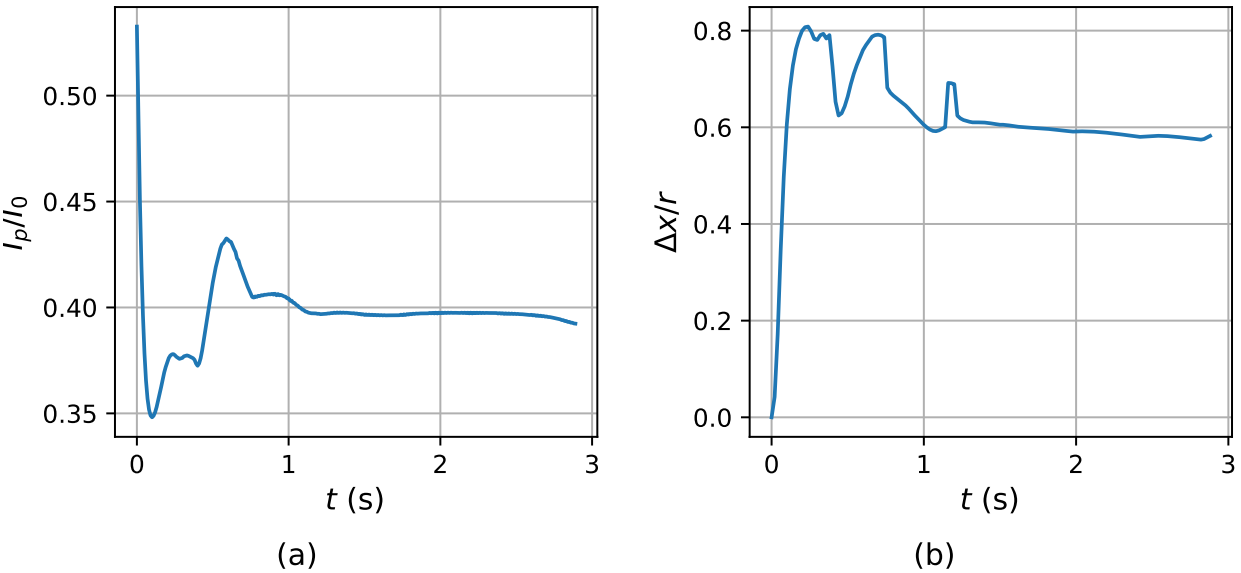

Fig. 9 Plot of (a) normalized peak intensity values and (b) normalized beam deflection over time in the $z = L_z$ plane.

We compared the laser beam intensity profile at $t = 1.5$ s from the simulation with that from the reference experiment in Fig. 10. At this time, the laser beam reaches the middle of the domain and exhibits almost steady-state behavior, as shown in Fig. 6 and Fig. 9. Since the experiment does not specify the exact time of the intensity profile, we assume it represents a steady-state profile as well. Considering the approximations in the governing equations and simulation parameters, the computed intensity profile shows satisfactory agreement with the experimental profile. We conducted simulations for other laser powers and velocities as described in the reference experiment. For higher laser velocities,

the system reaches steady-state, and the results align well with those reported in the experiment. However, for lower velocities, we were unable to achieve steady-state.

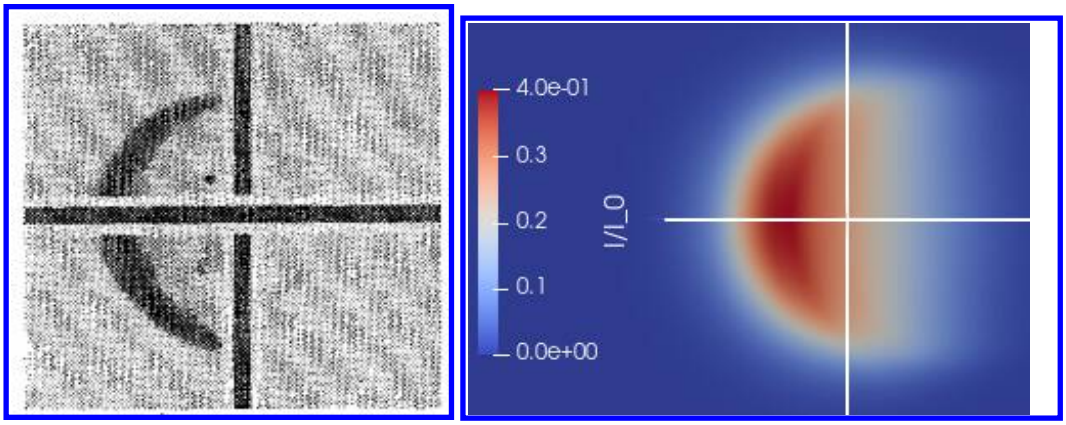

Fig. 10 Comparison of experimental [22] and computational laser beam intensity profiles in the $z = L_z$ plane.

V. Conclusion

To investigate laser-fluid interaction within closed domains, we developed a 3-D solver, icoLfiFoam. Within the OpenFOAM toolbox, we essentially augmented the built-in icoFoam fluid solver with capabilities for solving the coupled laser and fluid dynamics. We have validated the solver for two test cases:

1) Laser beam diffraction while propagating in a vacuum.
2) Thermal distortion of a laser beam propagating in the direction of gravitational force through a fluid cell, while moving at a constant velocity perpendicular to the beam propagation direction.

The obtained results are consistent with physical principles, and align closely with experimental findings available in the literature. We will use this solver to conduct a parametric study of the laser-fluid interaction in the closed domain. In the future, we plan to update the solver to solve the laser-fluid interactions in generalized domains and parallelize it in line with the other OpenFOAM solvers.

Appendix A: Laser beam attenuation effect in the paraxial equation

The paraxial equation in its nominal form is given by [23]:

$$2ik\frac{\partial A}{\partial z} = A_{xx} + A_{yy} + k^2\left(\frac{n^2}{n_0^2} - 1\right)A. \tag{12}$$

It is assumed that the rate of decrease in laser beam intensity along the beam propagation direction is directly proportional to the laser beam intensity:

$$\frac{dI}{dz} \propto -I. \tag{13a}$$

For a constant absorption coefficient β, this relationship can be expressed as

$$\frac{dI}{dz} = -\beta I. \tag{13b}$$

The paraxial equation is written in terms of the intensity amplitude A. Since

$$I = |A|^2, \tag{13c}$$

to satisfy Eq. 13b, the following must hold:

$$\frac{dA}{dz} = -\frac{\beta}{2}A. \tag{13d}$$

Thus, the paraxial equation, accounting for beam attenuation due to absorption, becomes:

$$2ik\frac{\partial A}{\partial z} = A_{xx} + A_{yy} + k^2\left(\frac{n^2}{n_0^2} - 1\right)A - ik\beta A. \tag{14}$$

Appendix B: Refractive index and temperature change relation

For small changes in refractive index and temperature:

$$n \approx n_0 + (T - T_0)\frac{dn}{dT}. \tag{15a}$$

For small changes, $\left|(T - T_0)\frac{dn}{dT}\right| << n_0$, we obtain:

$$n^2 \approx n_0^2 + 2n_0(T - T_0)\frac{dn}{dT}. \tag{15b}$$

Rearranging the terms of the above relation, we get:

$$\frac{n^2}{n_0^2} - 1 = 2\frac{(T - T_0)}{n_0}\frac{dn}{dT}. \tag{15c}$$

Appendix C: 1-D NLSE solution

The 1-D nonlinear Schrodinger (NLSE),

$$i\frac{\partial u}{\partial t} + u_{xx} + u|u|^2 = 0, \tag{16}$$

is a PDE similar to that of the paraxial equation. We have validated the implementation of split-step method by comparing the numerical solution of 1-D NLSE, solved using the split-step spectral method, against its exact solution [24]

$$u(t, x) = \sqrt{2}e^{i(0.5x+0.75t)}\text{sech}(x - t). \tag{17}$$

For $-10 \leq x \leq 10$, N = 100 and $\Delta t = 0.01$,the results show satisfactory agreement, as illustrated in Fig. 2.

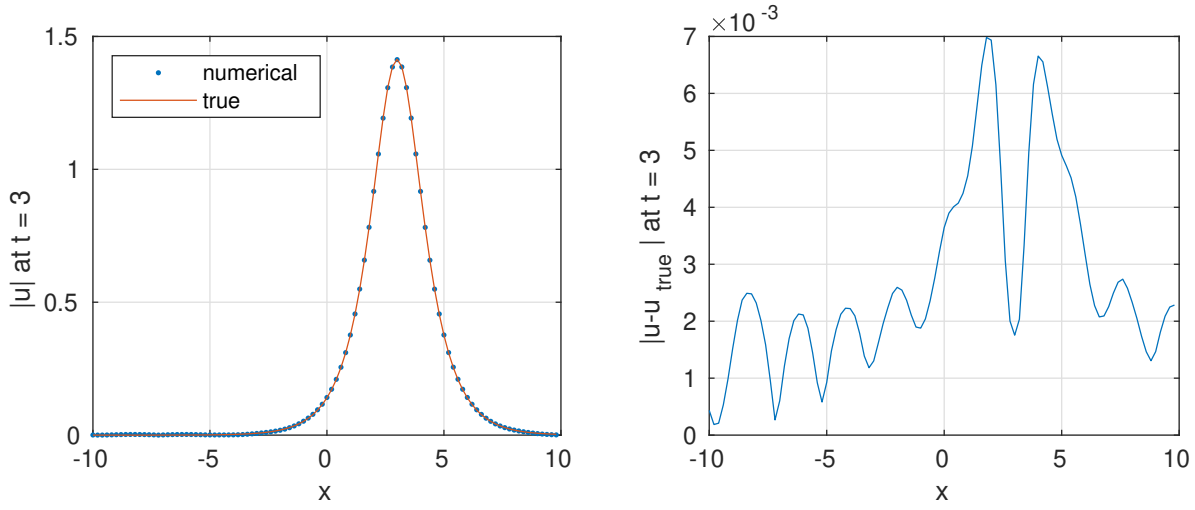

Fig. 11 Numerical solution of 1D NLSE, solved using the split-step spectral method, compared against its exact solution at t = 3 with a time step of Δt = 0.01.

Appendix D: Laser power and peak intensity relation for a Gaussian beam

The radius of a laser beam is defined as the distance from the peak of the beam to the points where the beam intensity is 1/e times its peak value. The intensity distribution of a Gaussian laser beam with radius r in radial coordinates is given by:

$$I = I_0 \mathrm{e}^{-\frac{r'^2}{r^2}}. \tag{18a}$$

For the laser beam of power P_0, we have

$$P_0 = \int_0^\infty I(2\pi r')\, dr' \tag{18b}$$

Substituting I into the integral:

$$P_0 = \int_0^\infty I_0 \mathrm{e}^{-\frac{r'^2}{r^2}} 2\pi r'\, dr' \quad = 2\pi I_0 \left| -\frac{r^2}{2} \mathrm{e}^{-\frac{r^2}{r^2}} \right|_0^\infty = \pi I_0 r^2. \tag{18c}$$

Thus,

$$I_0 = \frac{P_0}{\pi r^2}. \tag{18d}$$

References

[1] Thomas, D. J., "The effect of laser cutting parameters on the formability of complex phase steel," *The International Journal of Advanced Manufacturing Technology*, Vol. 64, 2013, pp. 1297–1311.

[2] Martukanitz, R. P., "A critical review of laser beam welding," *Critical Review: Industrial Lasers and Applications*, Vol. 5706, 2005, pp. 11–24.

[3] Michaelis, M. M., and Forbes, A., "Laser propulsion: a review," *South African Journal of Science*, Vol. 102, No. 7, 2006, pp. 289–295.

[4] Jin, K., and Zhou, W., "Wireless laser power transmission: A review of recent progress," *IEEE Transactions on Power Electronics*, Vol. 34, No. 4, 2019, pp. 3842–3859. https://doi.org/10.1109/TPEL.2018.2853156.

[5] Gebhardt, F. G., "Twenty-five years of thermal blooming: an overview," *Propagation of High-Energy Laser Beams Through the Earth's Atmosphere*, Vol. 1221, edited by P. B. Ulrich and L. E. Wilson, International Society for Optics and Photonics, SPIE, 1990, pp. 2 – 25. https://doi.org/10.1117/12.18326.

[6] Fleck, J. A., Morris, J., and Feit, M., "Time-dependent propagation of high energy laser beams through the atmosphere," *Applied physics*, Vol. 10, 1976, pp. 129–160. https://doi.org/10.1007/BF00896333.

[7] Wang, L., and Lin, W., "The effect of wind directions on the thermal blooming of a laser beam propagating in the air," *Journal of Russian Laser Research*, Vol. 37, 2016, pp. 407–410. https://doi.org/10.1007/s10946-016-9589-1.

[8] Ahn, K., Lee, S.-H., Park, I.-K., and Yang, H.-S., "Numerical simulation of high-energy laser propagation through the atmosphere and phase correction based on adaptive optics," *Journal of the Korean Physical Society*, Vol. 79, No. 10, 2021, pp. 918–929. https://doi.org/10.1007/s40042-021-00293-x.

[9] Zhang, Y., Ji, X., Li, X., and Yu, H., "Thermal blooming effect of laser beams propagating through seawater," *Optics Express*, Vol. 25, No. 6, 2017, pp. 5861–5875. https://doi.org/10.1364/OE.25.005861.

[10] Wang, L., and Lin, W., "The effect of the wind speed on the thermal blooming of a laser beam propagating in the rain," *Journal of Russian Laser Research*, Vol. 38, 2017, pp. 455–458. https://doi.org/10.1007/s10946-017-9666-0.

[11] Akers, B. F., and Reeger, J. A., "Numerical simulation of thermal blooming with laser-induced convection," *Journal of Electromagnetic Waves and Applications*, Vol. 33, No. 1, 2019, pp. 96–106. https://doi.org/10.1080/09205071.2018.1528183.

[12] Stephens, T., Johnson, D. C., and Languirand, M. T., "Beam path Conditioning for high-power laser systems," *The Lincoln Laboratory Journal*, Vol. 3, No. 2, 1990.

[13] Johnson, D. C., and Holderbaum, G. S., "Beam path conditioning for high energy laser beam directors," *Propagation Engineering: Third in a Series*, Vol. 1312, SPIE, 1990, pp. 422–442. https://doi.org/10.1117/12.21900.

[14] Tritton, D. J., *Physical fluid dynamics*, Springer Science & Business Media, 2012.

[15] "OpenFOAM/openfoam-10," , 2024. URL https://github.com/OpenFOAM/OpenFOAM-10, [Accessed 20-05-2024].

[16] Issa, R., Gosman, A., and Watkins, A., "The computation of compressible and incompressible recirculating flows by a non-iterative implicit scheme," *Journal of Computational Physics*, Vol. 62, No. 1, 1986, pp. 66–82. https://doi.org/10.1016/0021-9991(86)90100-2.

[17] Weller, H. G., Tabor, G., Jasak, H., and Fureby, C., "A tensorial approach to computational continuum mechanics using object-oriented techniques," *Computers in Physics*, Vol. 12, No. 6, 1998, pp. 620–631.

[18] Mross, C., *Numerical solutions to paraxial wave equations*, Master thesis, Delaware State University, 2018.

[19] Weideman, J. A. C., and Herbst, B. M., "Split-step methods for the solution of the nonlinear Schrödinger equation," *SIAM Journal on Numerical Analysis*, Vol. 23, No. 3, 1986, pp. 485–507. https://doi.org/10.1137/0723033.

[20] Frigo, M., and Johnson, S. G., "The design and implementation of FFTW3," *Proceedings of the IEEE*, Vol. 93, No. 2, 2005, pp. 216–231.

[21] Svelto, O., Hanna, D. C., et al., *Principles of lasers*, Vol. 1, Springer New York, NY, 2010.

[22] Gebhardt, F., and Smith, D., "Self-induced thermal distortion in the near field for a laser beam in a moving medium," *IEEE Journal of Quantum Electronics*, Vol. 7, No. 2, 1971, pp. 63–73.

[23] Strohbehn, J. W., *Laser beam propagation in the atmosphere*, Springer Nature, 1978.

[24] Schiesser, W. E., and Griffiths, G. W., *A compendium of partial differential equation models: method of lines analysis with MATLAB*, Cambridge University Press, 2009.